CHEMISTRY OF MATERIALS

ARTICLE

pubs.acs.org/cm

Stability of the $Sr_2B_3O_{6.5-\delta}$ Phases (B = Fe, Co, Ga): Existence Range, Structural and Physical Properties

H. Desmoulins, S. Malo,* O. Perez, D. Pelloquin, A. Maignan, and M. Hervieu

Laboratoire CRISMAT, UMR 6508 CNRS, ENSICAEN, 6 Boulevard du Maréchal Juin, 14050 Caen Cedex 4, France

ABSTRACT: A large solid solution $Sr_2(Fe_{3-x}Co_{x-y}Ga_y)O_{6.5-\delta}$, isostructural with the modulated Fe-2201 and Co-2201-type structures, has been characterized using X-ray powder diffraction (XRPD), transmission electron microscopy (TEM), and energy dispersive spectroscopy (EDS) analyses. The disorder phenomena have been studied using High Resolution Transmission Electron Microscopy (HREM). The evolution of the cell parameters, wavelength of the modulated structures, and transport properties are analyzed versus the three B (Fe, Co, Ga) cation contents, showing a violation of the Vegard law for a ratio Fe/(Fe + Co + Ga) close to $x \approx 0.6$. By decreasing the Fe content from that x value, an abrupt variation of resistivity of about 2 orders of magnitude is observed. This spectacular behavior is associated with the creation of percolative -(Co−O−Co)- pathways. A double effect of the (Co/Ga) substitution for Fe is observed on the magnetic properties. First, the B−O−B magnetic interactions (B = Fe, Co, Ga) are diluted because Ga^{3+} is a $d^{10}s^0$ cation and, second, the Co^{3+}−O−Co^{3+} magnetic exchange in that structure is smaller than the Fe^{3+}−O−Fe^3 ones. This explained why both the magnitude of the ferromagneto-like component and the T_N values are reduced as compared to the Fe-2201′s.

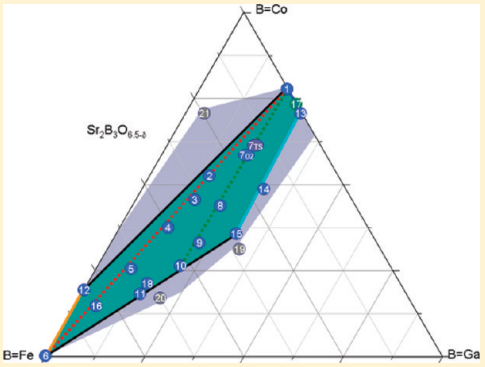

KEYWORDS: doped strontium ferrites/cobaltites, pseudoternary diagram, transmission electron microscopy, 2201-type modulated structure, transport properties

INTRODUCTION

Cobaltites and ferrites form large families of oxides, which received for a long time a large amount of interest because of their wide range of remarkable physical properties; this interest is still increasing with the discovery of new materials having the original frameworks. Among them, one family of layered compounds is of importance by its structural relationships with the high temperature superconductor cuprates (HTSC), characterized by the intergrowth of m ABO_3 perovskite layers with one block of n rock salt (RS)-type layers ($n = 2$ and $n = 3$, respectively).[1,2] For the different [$n = 3$, $1 \le m \le 5$] members, a simplified notation using four numbers $(n-1)2(m-1)m$ commonly replaces the complex $A'_2Sr_2A_{m-1}B_mO_{3m+3}$ formulation.[1] The B atoms are transition metals (Cu,[1−3] Co,[4] Fe,[5,6] and Mn[7] for the 2201′s) and A′ atoms are generally $5d^{10}6s^2$ cations such as Bi, Tl, Pb, and also Hg (possibly partly substituted by alkaline earth or B). The exceptional character of the Bi−Sr−Fe−O system lies in the existence of two families of layered compounds: the $Bi_2Sr_2A_{m-1}Fe_mO_{3m+3+\delta}$ (A = Sr, Ca) family, denoted Bi-22-$(m-1)m$,[5,6] and the $Fe_2A'_2Sr_{m-1}Fe_mO_{3m+3.5-\delta}$[8−13] (A′ = Bi, Sr) members, denoted Fe-22$(m-1)m$, respectively. The $\boldsymbol{m} = 1$ member of the second family, $Sr_2Fe^{3+}_3O_{6.5}$, exhibits an average structure first described[11−13] on the basis of a stoichiometric oxygen content for trivalent B cations and the orthorhombic unit cell, with $a \approx 2\,a_p\sqrt{2}$, $b \approx a_p\sqrt{2}$ (a_p is the parameter of the perovskite unit cell), $c_{2201} \approx 19$ Å. Further transmission electron microscopy studies evidenced the actual modulated character of the $Sr_2Fe_3O_{6.5-\delta}$ derivatives[14−18] and the isostructural $Sr_2(Ga_{1/3}Co_{2/3})_2CoO_{6.5-\delta}$ (Co-2201),[19] with wavelengths directly correlated with the oxygen content. Another example of this correlation is observed in the stoichiometric In-2201 compound $Ba_2In_3O_{6.5}$,[20] which exhibits the orthorhombic cell ($2\,a_p\sqrt{2} \times a_p\sqrt{2} \times c_{2201}$) but incommensurate modulated structures by Mg^{2+} doping for In^{3+}.

In the present paper, we present the investigation of the existence domain of the B-2201-type phase, $Sr_2B_3O_{6.5-\delta}$, with B^{3+} = Fe, Co, Ga, by scanning a ternary diagram based on the three B metal oxides. A large solid solution $Sr_2[Fe_{3-x}(Co_{x-y}Ga_y)]O_{6.5-\delta}$ has been characterized, using X-ray powder diffraction, transmission electron microscopy, and energy dispersive spectroscopy analysis. The evolution of the cell parameters and wavelength of the modulated structures is given. We show the effect of the joined introduction of Co and Ga instead of Fe in the $Sr_2Fe_3O_{6.5-\delta}$ phase upon the structural, magnetic, and electronic properties.

EXPERIMENTAL SECTION

Synthesis. The $Sr_2(Fe_{3-x}Co_{x-y}Ga_y)O_{6.5-\delta}$ samples have been prepared by scanning the ternary diagram "$Sr_2Fe_3O_{6.5}$-$Sr_2Co_3O_{6.5}$-$Sr_2Ga_3O_{6.5}$" Different thermal processes similar to those reported for the two limit compounds, Fe-2201[13,15] and Co-2201,[19] have been considered for the first investigations (XRPD and EDS) in the present

Received: December 21, 2010
Revised: April 20, 2011
Published: May 16, 2011

diagram; they confirmed the high sensitivity of the sample homogeneity to the thermal process and oxygen pressure. We have then retained two different synthesis processes applied to all the compositions. In the first process, $SrCO_3$, $CoO_{4/3}$, Fe_2O_3, and Ga_2O_3 were intimately mixed in an agate mortar. The samples were fired in alumina crucibles at 900 °C for 12 h, for decarbonation, pressed in the form of bars ($2 \times 2 \times 10$ mm^3) and, last, reacted in an oxygen flow for 24 h at 1100 °C. In the second process, the stoichiometric amounts of SrO_2, SrO, $CoO_{4/3}$, Fe_2O_3, and Ga_2O_3 have been introduced in a sealed silica tube, after pressed in bars. The heating temperature was increased up to 1100 °C in 12 h and maintained for 24 h at that temperature.

Single crystals were grown starting from $SrCO_3$, $CoO_{4/3}$, Fe_2O_3, and Ga_2O_3 in the stoichiometric proportions. After decarbonation, the mixtures (about 8 g) were introduced in alumina tubes deposited in a vertical sealed silica ampule. The temperature was increased (100°/h) up to 1250 °C, maintained at this temperature for 24h, decreased at 1200 °C, then to 1000 °C (2°/h), with a palier of 24 h, and last decreased down to room temperature (100 °C/h). The structural characterization of the single crystals using the superspace formalism[21] will be reported elsewhere, but we used the as-refined parameters for the calculated electron microscopy images displayed in the present paper.

Transmission Electron Microscopy. Each of the as-synthesized samples was systematically analyzed by coupling electron diffraction (ED) and Energy Dispersive Spectroscopy analyses, using JEOL 200CX and JEOL 2010 transmission electron microscopes. The high-resolution electron microscopy study was carried out with a JEOL 2010F transmission electron microscope (Cs = 1 mm). For the TEM studies, a small piece of sample was crushed in an agate mortar containing *n*-butanol and a droplet was deposited on a copper grid covered with holey carbon film. For commensurate modulated structures, image calculations were carried out with the Mac Tempas and JEMS software considering a superstructure.

X-ray Diffraction. The X-ray powder diffraction study was carried out at room temperature using a X-pert Pro (Panalitycal) vertical diffractometer working with the Cu−Kα radiation and equipped with an X′ Celerator detector. Data were collected by 0.017° (2θ) step from 4° to 120°.

Transport and Magnetic Measurements. The electrical resistivity was measured by the four-probe technique using four ultrasonically deposited indium contacts. The bars were glued by using a GE varnish on the samples. The magnetic properties were measured with the ACMS option of the physical properties measurements system (PPMS Quantum Design) operating from 5 K to 400 K. The alternating current (ac) susceptibility was measured with $f = 10^4$ Hz and $\mu_0 h_{ac} = 10^{-3}$ T.

RESULTS

State of the Art. In the ideal B^{3+}-2201 structure, one perovskite-type slice $[ABO_3]_\infty$ (A = Sr, Ba ; B = Co, Fe, Ga, In, and so on) alternates, along $\vec{c}$, with one complex block, built up from a double layer $[B_2O_{2.5}]_\infty$ sandwiched between two [AO] layers (Figure 1a); this is the case of $Ba_2In_3O_{6.5}$.[20] In the Fe-2201′s and Co-2201′s, the modulated structures are characterized by the vector, $\vec{q} = p\vec{a}^* + r\vec{c}^*$: the component p varies with the oxygen stoichiometry as $p = (1/2 - \delta)$ and the second component is $r = 1$ in both compounds.[14−19] Under our previous processing conditions, the structure of $(Fe)_2Sr_2FeO_{6.5-\delta}$ is incommensurate with $0.4 \leq p \leq 0.46$ and commensurate for $(Ga_{1/3}Co_{2/3})_2Sr_2CoO_{6.33}$ (Figure 1a) with $p = 1/3$. In these compounds, the modulated character originates from the oxygen content of the double layers according to the formulation $[B_2O_{2.5-\delta}]_\infty$. At present, the structure refinements carried out on different Fe-2201 and Fe-2212 compounds using a superspace

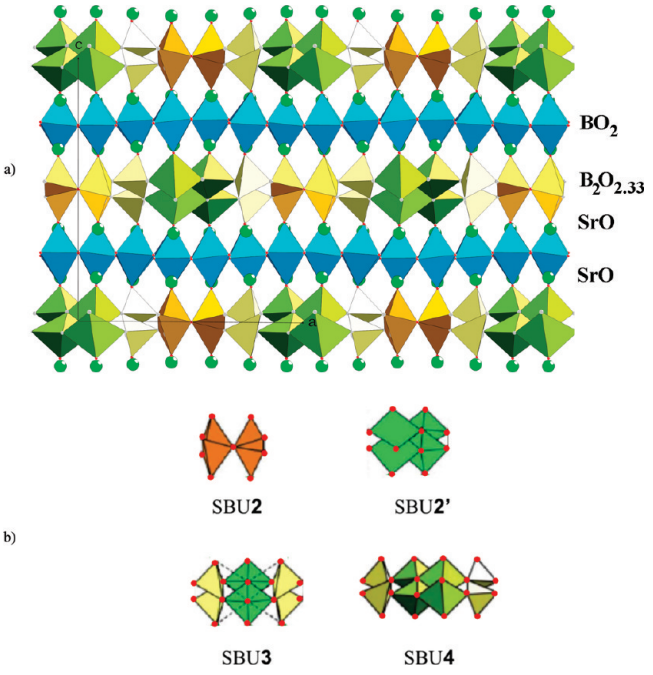

Figure 1. (a) Structure of the $Sr_2B_3O_{6.33}$ commensurable 2201 phase projected along [010] (B = Co, Ga) and (b) SBUs.

formalism[21] showed that the B cations adopt four types of coordination:[17] octahedra in the perovskite layer and trigonal bipyramids (TBP), tetragonal pyramids (TP) and monocaped tetrahedra (MT) in the double layer $[B_2O_{2.5-\delta}]_\infty$ (Figure 1b). Four types of structural building units (*SBU*), made of **2**, **3**, or **4** edge- and corner-sharing polyhedra allow therefore to describe the complex block $[SrB_2O_{3.5-\delta}]_\infty$ sandwiching the perovskite layers.[17] One *SBU2* made of two trigonal bipyramids (TBP) systematically alternates with one of the three following units: *SBU2′* made of two tetragonal pyramids (TP), *SBU3* built up from one (TP) sandwiched between two monocaped tetrahedra (MT) or *SBU4* built up from 2(TP) sandwiched between two (MT) (Figure 1b). The simplest commensurate structures can be described from ordered sequences of *SBU*s: (*SBU2* +*SBU2′*) for $p = 1/2$, (*SBU2* +*SBU3*) for $p = 2/5$, and (*SBU2* +*SBU4*) for $p = 1/3$. In the incommensurate structures the regularity of the polyhedra sequence is broken. Owing to the mismatch observed between the periodicities of the subcell and the one of the modulation, the short-range order is lost although the long-range order is still observed. The resulting sequence is more complex; an ad hoc periodic insertion of SBU motifs in the sequence observed for the commensurate cases allows the generation of the incommensurate structure. Thus, the $p = 0.46$ case derives from the $p = 1/2$ case by the periodic insertion of (*SBU2* +*SBU3*) blocks.

(I). Existence Range of the B-2201-Type Structure $Sr_2(Fe_{3-x}Co_{x-y}Ga_y)O_{6.5-\delta}$. As mentioned in the Experimental Section, a first-step study has been applied to all the samples by coupling XRPD, electron diffraction and EDS analyses on numerous crystallites. The sample homogeneity was tested by EDS analyses through the Sr/Fe/Co/Ga ratio of every crystallite whereas the coupled ED study allows to check the structural-type and to measure the component p of the modulation vector of the B-2201 phases. Both techniques allowed to detect impurities (even in small amount). In a general way, the best results have been obtained for the samples prepared under

dx.doi.org/10.1021/cm103635g |*Chem. Mater.* 2011, 23, 2786–2794

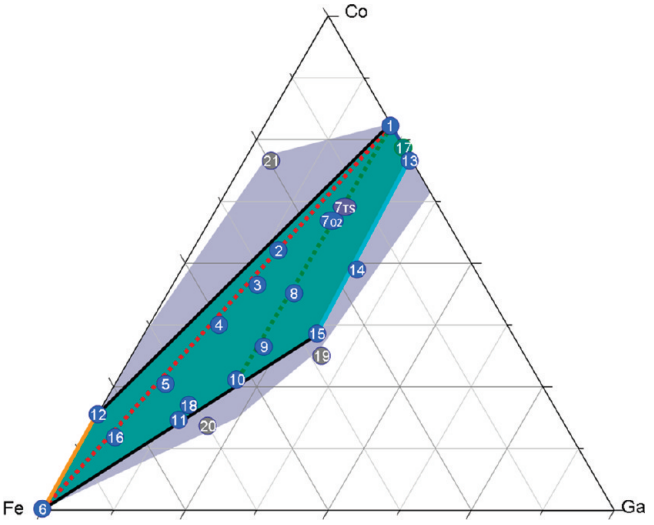

Figure 2. Existence range of the B-2201 phases for $R_{B/Sr}$= 1.5. The green domain corresponds to single phased samples.

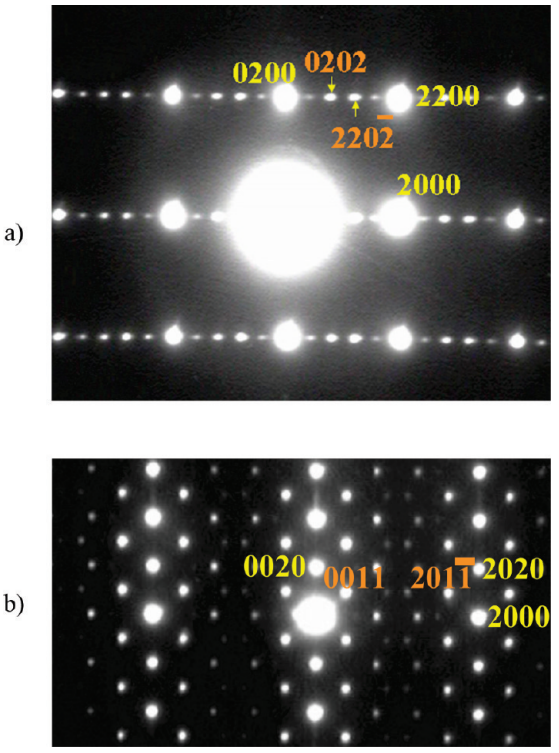

Figure 3. (a) [001] and [010] (b) ED patterns with p = 0.38 (**#11:** $Ga_{0.45}Co_{0.55}Fe_2O_{6.38}$). The indexations of the reflections, using four *hklm* indices ($\vec{q} = p\vec{a}^*$) are schematically drawn besides the experimental patterns: the colors are associated with one reflection of the subcell and its satellite.

oxygen flow. The ratio $R_{B/Sr}$ = [Fe + Co + Ga]/[Sr] (theoretically $R_{B/Sr}$= 1.5) has been determined from EDS analyses for each of the synthesized samples. The ternary diagram "$Sr_2FeO_{3.5}$-$Sr_2CoO_{3.5}$-$Sr_2GaO_{3.5}$" (Figure 2) is representative of the relative ratios of the three cations located in the B sites of a B-2201 structure (numbered in the diagram) and discussed in this paper.

(i). Electron Diffraction Study: The Modulation $\vec{q} = p\vec{a}^*$. For every crystallite, the components of the modulation vector

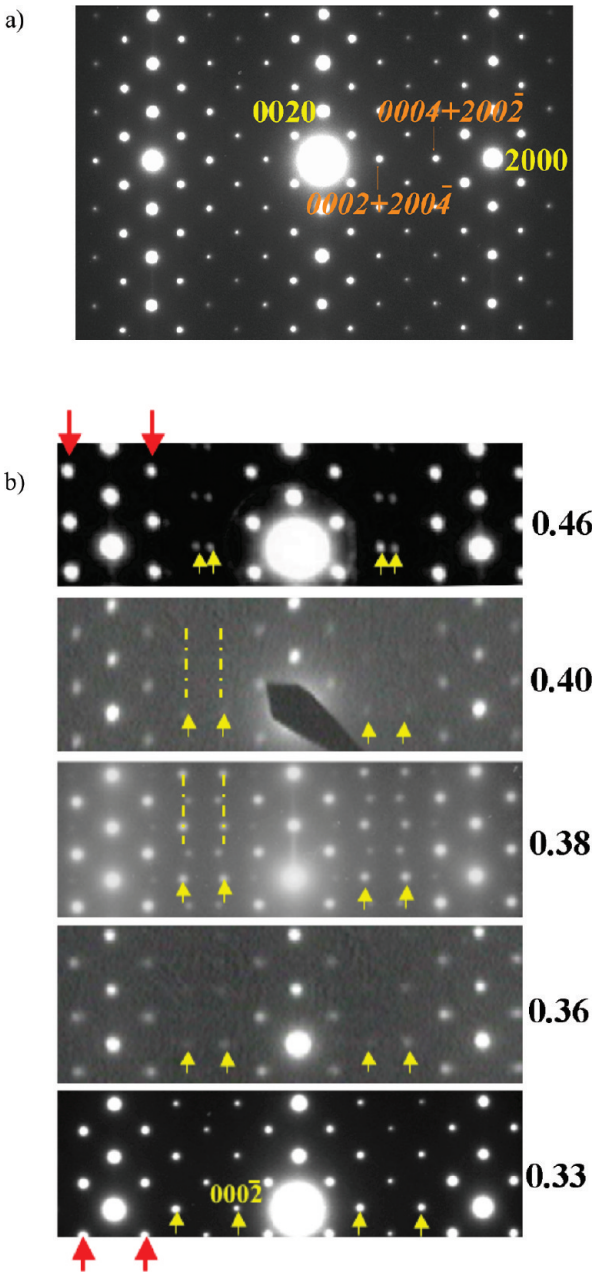

Figure 4. (a) [010] ED pattern of the compound (**#15:** $Sr_2Co_{1.05}Ga_{0.9}Fe_{1.05}O_{6.33}$) with p = 1/3. The superposition of the satellites is typical of a commensurate modulated structure; (b) evolution of the positions of the spots vs p along $\vec{a}^*$.

$\vec{q} = p\vec{a}^* + r\vec{c}^*$ were determined by measurements on the [010] and [001] electron diffraction (ED) patterns. The r value remains constant, r = 1, whereas p varies with the cation composition and the oxygen content, depending on the synthesis process. For simplifying the expression of the symmetry operators, the following centering lattice {1/2 1/2 0 0; 1/2 0 1/2 1/2; 0 1/2 1/2 1/2} has been adopted in the superspace; the vector becomes then $\vec{q} = p\vec{a}^*$.

Whatever the lines of the diagram (Figure 2), the component p decreases as the Co and Ga contents increase. Starting from Fe-2201 (sample **#6**), p decreases from 0.46 down to 0.41 for the Ga-free compounds (**#12**), and down to p = 1/3 for the iron-free compound (**#1**). Two typical examples are given in Figures 3

dx.doi.org/10.1021/cm103635g |*Chem. Mater.* 2011, 23, 2786–2794

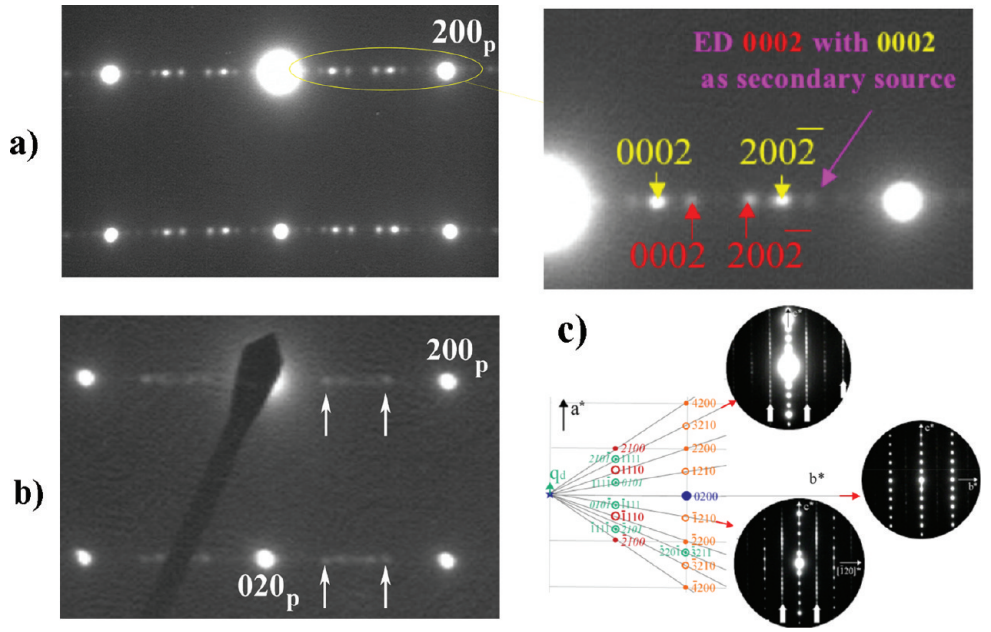

Figure 5. [001] SAED patterns of crystallites with two modulation vectors: (a) $p_1 = 0.31$ (yellow indices) and $p_2 = 0.41$ (red indices) #7) and (b) $p_1 \approx 0.33$ (white arrows) and $p_2 = 0.44$, note the diffuse streaks in the rows parallel to [100]* (**#11:** $Ga_{0.45}Co_{0.55}Fe_2O_{6.38}$). (c) Commensurate structure ($p = 1/3$): reconstruction of the reciprocal space by tilting around $\vec{c}^*$ and enlargement of three selected ED patterns. The additional point-like spots of associated to the second ordering phenomenon (spots of (h0l) and (h2l) are open green circles and (h11) full green circles).

(**#11**) and 4 (**#15**). The [010] (Figure 3a) and [001] (Figure 3b) ED patterns are characteristic of incommensurate structures with $p = 0.38$ (**#11**); the intense spots are those of the subcell and the weaker ones are satellites, all indexed using four *hklm* indices. The unequal spacing of the satellites is the signature of incommensurate modulations but the superimposition of the satellites 0004 with $200\bar{2}$ and 0002 with $200\bar{4}$ (Figure 4a, $p = 1/3$ for sample **#15**) is typical of a commensurate modulated structure. This $p = 1/3$ compound could be indexed in an orthorhombic 3D supercell considering a tripling of the ***a*** parameter. The second example (Figure 4b) presents the evolution, versus the p values, of the spots positions along $\vec{a}^*$ in the [010] ED patterns, as observed in the ternary diagram as the Fe content decreases.

Increasing the Ga content in the iron free cobaltite $Sr_2Ga_{0.92}Co_{2.08}O_{6.5-\delta}$ (**#13**) retains an average p value close to 1/3 but induces an incommensurate character of the modulations with $p = 0.33 \pm 0.02$. In the solid solutions with a constant Ga content, the p value varies only slightly from 0.33 to 0.36 for the line **#1** to **#10** and remains almost constant for the line **#13** to **#15** (see further their cell parameters evolutions).

As mentioned before, TEM studies[14−18] showed that the incommensurate character of the modulation is associated with broken sequences of *SBU*s in the double layer $[B_2O_{2.5-\delta}]$ along $\vec{a}$. For homogeneous B-2201 particles, the calculated p value of the local sequences, recorded at the scale of a few tens nanometers, is generally close to the average value of the whole sample. However, in a few crystallites, segregation mechanisms can be observed with the presence of zones characterized by two different p values. As an example, the average p value of the sample (#7) is 0.35 ± 0.02 but one of the crystallites exhibits two superimposed systems of satellites with $p_1 = 0.31$ (yellow indices) and $p_2 = 0.41$ (red indices). The indexation of such ED patterns is complicated by the double diffraction effects of the p_2 system, as presented in Figure 5a with the 0002 satellite of the p_1 system as secondary source. In the second example (Figure 5b), besides the satellites associated with $p_1 \approx 0.33$ (white arrows) and $p_2 = 0.44$, diffuse streaks are observed in the rows parallel to the $\vec{a}^*$ axis (**#11** for an average value $p = 0.38$). In such crystallites, the mechanisms of segregation induce different nanostructural states. This point will be discussed in the HREM section.

(ii). Second Ordering Phenomenon and Diffuse Scattering. In the case of the commensurate structure $p = 1/3$, the intense reflections and satellites can be indexed in the supercell $a_{sup} \approx 3a_p\sqrt{2} \approx 16.43$ Å, $b_{sup} \approx a_p\sqrt{2} \approx 5.52$ Å, and $c_{sup} \approx 19.13$ Å. However, additional spots, associated to diffuse scattering lines parallel to $\vec{c}^*$, are observed in the ED patterns (see white arrows in Figure 5c). The reconstruction of the *(001)** plane, as those of the upper layers, obtained for commensurate crystal ($p = 1/3$) by tilting around $\vec{c}^*$, is given in Figure 5c; the additional point-like spots are drawn as open green circles for the *hk0* and *hk2* spots and as full green circles for the *hk1* ones. The positions of the diffuse lines imply a doubling of the ***a*** parameter ($a_{order} \approx 6a_p\sqrt{2} \approx 33$ Å) while their diffuse character are the signature of a loss of coherency along $\vec{c}$. Determining the origin of these phenomena needs the refinement of single crystal XRD data, using a superspace formalism.[21]

(iii). Homogeneity Range. The whole ternary diagram has been investigated. Following our synthesis modes, two domains can be defined, as drawn in Figure 2: the green zone is associated to the domain of single-phased samples, whereas the purple zone is the limit of existence of the B-2201 phases characterized by inhomogeneous or multiphased samples. The interest of the latter domain is to suggest that the B-2201 homogeneity range could be enlarged; only the first domain is detailed herein. Note that, contrary to the limit compounds $Sr_2Fe_3O_{6.46}$ (**#6**) and $Sr_2Ga_{2/3}Co_{7/3}O_{6.33}$ (**#1**), we cannot specify the repartition of each of the three B cations over the RS and perovskite sites of the B-2201 structure; therefore, the general formulation $Sr_2Fe_{3-x}(Co_{x-y}Ga_y)O_{6.5-\delta}$ is used without differentiating the B cations in the perovskite and RS layers.

dx.doi.org/10.1021/cm103635g |*Chem. Mater.* 2011, 23, 2786–2794

Table 1. Selected Solid Solutions of the B-2201-Type Structure in the Diagram (Figure 2)

solid solution	x limit values	line of the diagram
$Sr_2(Fe_{3-x}Ga_x)O_{6.5-\delta}$	0	**#6**
$Sr_2(Fe_{3-x}Co_x)O_{6.5-\delta}$	$0 \le x \le 0.6$	**#6** to **#12**
$Sr_2(Co_{7/3-x}Ga_{2/3+x})O_{6.5-\delta}$	$0 \le x \le 0.26$	**#1** to **#13**
$Sr_2(Fe_{3-x}(Co_{7/3}Ga_{2/3})_x)O_{6.5-\delta}$	$0 \le x \le 3$	**#6** to **#1**
$Sr_2(Fe_{3-x}Co_{x-2/3}Ga_{2/3})O_{6.5-\delta}$	$1.6 \le x \le 3$	**#1** to **#10**
$Sr_2(Fe_{3-x}Co_{x-0.9}Ga_{0.9})O_{6.5-\delta}$	$1.95 \le x \le 3$	**#13** to **#15**

The actual homogeneity domain of the $Sr_2Fe_{3-x}(Co_{x-y}Ga_y)O_{6.5-\delta}$ phase is large; curiously, the synthesis of Co-free sample $Sr_2(Fe_{3-x}Ga_x)O_{6.5-\delta}$ is the only one that failed, multiphased samples being observed as soon as Ga substitution is attempted. The limits of the main solid solution are summarized in Table 1. According to our processes, the solid solution $Sr_2(Fe_{3-x}Co_x)O_{6.5-\delta}$ is limited to $x \approx 0.2$ (**#12**), the perovskite $SrFe_{1-x}Co_xO_3$ being detected by EDS and ED as $x > 0.2$. The different limits reported for it[22−24] can be correlated with the various synthesis modes used by the authors and the difficulty to detect the formation of the perovskite in XRPD patterns because of the superimposition of the main peaks. However, it is important to note that the Co-richest B-2201crystallites containing Fe (**#21**) exhibit compositions close to $Sr_2(Fe_{0.75}Co_{2.15}Ga_{0.1})O_{6.5-\delta}$ (with $p \approx 0.33$) showing that 3% of Ga is able to stabilize a high Co content in the Fe/Co-2201′s.

The iron-free solid solution $Sr_2(Co_{7/3-y}Ga_{2/3+y})O_{6.5-\delta}$ is extended up to $y = 0.26$ (**#13**). $Sr_2(Fe_{1.05}Co_{1.05}Ga_{0.9})O_{6.33}$ (**#15**), which exhibits the constant maximum Ga content (30%), is the limit point of the solid solution $Sr_2(Fe_{3-x}Co_{x-0.9}Ga_{0.9})O_{6.5-\delta}$ and close to the limit of the purple diagram, $Sr_2(GaCoFe)O_{6.5-\delta}$ (**#19**), barycenter of the diagram. Two solid solutions, $Sr_2Fe_{3-x}(Ga_{2/3}Co_{7/3})_xO_{6.5-\delta}$ (line **#1** to **#6**, crossing the whole diagram) and $Sr_2(Fe_{3-x}Co_{x-2/3}Ga_{2/3})O_{6.5-\delta}$ (line **#1** to **#10** with Ga/(Fe + Co + Ga) = 2/9), have focused our attention because they show the peculiar evolution of the cell parameters and transport properties.

Remarks on the Cation and Oxygen Stoichiometry. For certain powder samples, whatever their synthesis process, the actual average ratios $R_{B/Sr}$ have been observed slightly larger than 1.5, which involves a Sr nonstoichiometry with regard to the ideal ratio of a B-2201 phase and the formulation $Sr_{2-\varepsilon}B_3O_{6.5-\delta}$ for a fully occupancy of the B sites. Varying the precursors and annealing treatments showed that this $R_{B/Sr}$ ratio can be slightly modified and the EDS analyses confirmed that the Sr content could be varied between 2 and 1.85 ($\Delta Sr/Sr = 0.075$), which is higher than the limit of the experimental error. This observation raises the question of the oxygen content of these B-2201′s. For the first limit Fe-2201 (**#6**), the value $p = 0.46$ implies the formula $Sr_2Fe_3O_{6.46}$ ($p = 1/2 - \delta$) and the chemical titration gave oxygen content close to 6.5.[17] Both results lead to an iron oxidation number close to +3, consistent with the synthesis process carried out under an oxygen flux and, therefore, with the intergrowth of one $SrB_2O_{3.46}$ complex block with one stoichiometric $SrBO_3$ perovskite layer. For the Co-2201′s with $p = 1/3$, an oxygen content of 6.33 implies a calculated oxidation state of Co close to +2.85, assuming Ga^{3+}. In other words, a trivalent B^{3+} cation in the $Sr_2B_3O_{6.33}$ compound is incompatible with $p = 1/3$, even considering a Sr-deficient phase. Different hypotheses can be put forward to express these relationships between these parameters, considering either a cation redistribution or an actual cation deficiency. For a $Sr_{1.85}\square_{0.15}B_3O_{6.33}$ sample

- the hypothesis **1** of a cation redistribution leads to the formulation $(Sr_{1.9}B_{0.1})B_3O_{6.33}$ with the localization of a part of the B cations over the vacant Sr sites,
- the hypothesis **2** of an actual cation deficiency leads to the formulation $Sr_{2-\varepsilon}B_{3-\varepsilon'}O_{6.33}$.

These mechanisms allow to account an adequate ratio ΣB/Sr = 1.5 up to 1.62. As examples the four limit compositions deduced from these limit formulations are given in Table 2 for compounds having a modulation vector $p = 1/3$. The first solution induces a potential reduction of at least one of the B cations, even if one of the cation (likely Co) suffers disproportionation, but appears rather unlikely in an oxidizing process whereas the second one retains the average trivalent oxidation state of the B cations. Powder XRD data refinements cannot provide any answer to this problem.

A deviation of the cation stoichiometry, with regard to the theoretical one, has been also reported in the barium based In-2201 compound $Ba_2In_{3-x}O_{6.5-0.75x}$.[20] However, its nonstoichiometry mechanism concerns the B cations and the x value remains very weak ($x_{max} = 0.025$). These different behaviors are consistent with the ability of the Fe and Co cations to easily take different valences, compared to the In cations. These results suggest that the existence domain displayed in Figure 2 is more complex with an extent in the quaternary diagram, in which the ratio [(Fe + Co + Ga)/Sr] can vary ($1.5 \le \Sigma B/Sr \le 1.6$). This extent has not been fully investigated.

(iv). Subcell Parameters of the B-2201 Compounds. The subcell parameters have been refined from the XRPD data. The refined values of several compounds are reported in Table 3, and the parameters' evolution versus x is given in Figure 6 for lines (**#1**−**#10**) and (**#6**−**#1**); the conclusions are similar for the other lines of the diagram. In the whole domain $Sr_2(Fe_{3-x}Co_{x-y}Ga_y)O_{6.5-\delta}$, decreasing the oxygen content leads to an increase of the ***c*** parameter and a decrease of ***a*** and ***b***. The ***b/a*** ratio increases with the Ga content along the different lines from 1.004 for the iron compound (**#6**) to ≈1.007 for the Fe free compounds (line **#1**−**#13**); it is maximum for **#15**, $Sr_2Ga_{0.9}Co_{1.05}Fe_{1\cdot05}O_{6.5-\delta}$, with a Ga content close to the third of the B cations. However, if the common evolution in the whole domain is an increase of the ***c*** parameter as iron content decreases, one interesting peculiarity is observed. As observed in Figure 6 for the $Sr_2Fe_{3-x}(Ga_{2/3}Co_{7/3})_xO_{6.5-\delta}$ ((**#6**−**#1**) line, a slope breaking is observed in the evolution of ***a, b, c*** and p parameters versus x close to the point **#5**; this corresponds to a ratio Fe/(Co + Ga) close to 0.6. This evolution is confirmed through the inner points, not presented herein, of the diagram (as for $Sr_2Fe_{3-x}Co_{0.538x}Ga_{0.461x}O_{6.5-\delta}$ (**#6**−**#15**)).

As the Vegard law is violated, this variation could be correlated with a preferential occupancy of the RS and perovskite layers by specific B cations for $x > 0.6$, that is, as soon as the ratio (Ga + Co)/Σ*B* is larger than 0.4. In $Sr_2Fe_3O_{6.46}$ (**#6**), only one kind of cation occupies the two types of layers whereas, in $Sr_2(Ga_{2/9}Co_{7/9})_3O_{6.33}$ (**#1**), a cation ordering is observed with $(Ga_{1/3}Co_{2/3})_2$ in the RS layer and (Co) in the perovskite one. Starting from Fe-2201, these breaking points could be associated with the appearance of a partial cation ordering.

(II). High-Resolution Electron Microscopy Study. *(i). Commensurate and Incommensurate Structures.* The nanostructural states of these B-2201 compounds have been characterized as a function of the Fe and (Co/Ga) contents by high-resolution

dx.doi.org/10.1021/cm103635g |*Chem. Mater.* 2011, 23, 2786–2794

Table 2. Four Limit Formulations for Compounds Having a Modulation Vector $p = 1/3$

EDS analyses	limit formulation Hyp. **1**	calculated O.N. hyp. **1**	limit formulation Hyp. **2**	calculated O.N. hyp. **2**
Sr-stoichiometry: $Sr_2B_3O_{6.33}$	$Sr_2B_3O_{6.33}$	+2.89 * 2.86 for **#1**	$Sr_{1.95}B_{2.92}O_{6.333}$	+3
Sr-deficient $Sr_{1.85}B_3O_{6.33}$	$(Sr_{1.9}B_{0.1})B_3O_{6.33}$	+2.86	$Sr_{1.88}B_3O_{6.33}$	+3

Table 3. Subcell Parameters and p Components of the B-2201-Type Structure

compositions	No.	a modul	b	c	p	$\rho_{300\ K}$ (Ω cm)	E_a (meV)
$Sr_2Fe_3O_{6.46}$	**#6**	5.552(1)Å	5.574(1)Å	18.938(1)Å	0.46	10710	289
$Sr_2Fe_{2.4}Co_{0.6}O_{6.46}$	**#12**	5.5337(1)Å	5.563(1)Å	19.004(1)Å	0.41	5739	234
$Sr_2Co_{1.05}Ga_{0.9}Fe_{1.05}O_{6.33}$	**#15**	5.476(1)Å	5.521(1)Å	19.130(1)Å	0.333	263.5	244
$Sr_2Co_{1.8}Ga_{0.72}Fe_{0.5}O_{6.36}$	**#7**	5.448(1)Å	5.490(1)Å	19.175(1)Å	0.36	2.3	139
$Sr_2(Co_{7/9}Ga_{2/9})_3O_{6.33}$	**#1**	5.434(1)Å	5.4725(1)Å	19.203(1)Å	0.333	1.40	74
$Sr_2(Co_{0.69}Ga_{0.31})_3O_{6.33}$	**#13**	5.440(1)Å	5.475(1)Å	19.186(1)Å	0.333	0.28	124

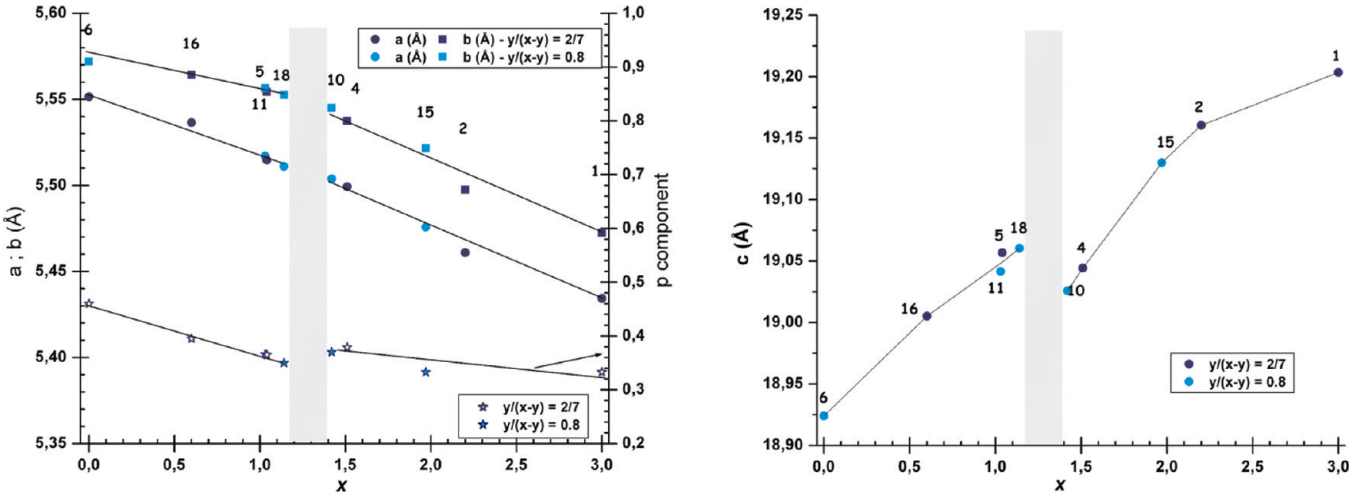

Figure 6. $Sr_2(Fe_{3-x}Co_{x-y}Ga_y)O_{6.5-\delta}$ for $y/(x-y) = 0.2/7$ and 0.8: unit cell parameters evolution vs x of (a) a, b and p and (b) c.

electron microscopy (HREM). In so complex materials, where the three B cations have close atomic numbers and the positions of the oxygen atoms in the double layer $[B_2O_{2.5-\delta}]_\infty$ have a crucial incidence on the contrast, the interpretation of such image contrast needs to be confirmed by image calculations, using accurate positional parameters that can only be obtained from refinements of single crystal XRD data or coupled single crystal XRD/neutron diffraction data. The results obtained for the two limit compounds (**#6**) with $p = 0.46$ and (**#1**) with $p = 1/3$ have been previously reported[17,19] so that single crystal growths have been carried out for mixed compositions of the diagram: $Sr_2Fe_{2.15}Co_{0.55}Ga_{0.3}O_{6.5-\delta}$ (iron rich and incommensurate) and $Sr_2Fe_{0.95}Co_{1.25}Ga_{0.8}O_{6.5-\delta}$ (Co rich and commensurate) close to **#11** and **#8**, respectively. Their refined structures in the superspace formalism and the origins of the disorder mechanisms, generating diffuse scattering, will be detailed elsewhere. However, supercell can be proposed to describe a commensurate structural form. In this commensurate case ($p = 1/3$), a model has been built and refined from single crystal XRD data. In Figure 7a, the (010) image recorded for the compound **#8** is typical of commensurate modulated structures with $p = 1/3$ (the corresponding ED pattern is in Figure 4a). Theoretical images were calculated using the positional parameters refined for the $Sr_2Fe_{2.15}Co_{0.55}Ga_{0.3}O_{6.33}$ single crystal and compared to the experimental ones. For a focus value close to Scherzer $\Delta f = -610$ Å and crystal thickness of 33 Å, the positions of the Sr cations appear as the darkest dots. At the level of the double layer $[B_2O_{2.5-\delta}]_\infty$ of the RS block, the small grayer dots are correlated with the positions of the double trigonal bipyramids (*SBU2*) sharing one oxygen atom. In between these two gray dots, four darker ones are associated with the other polyhedra of the double layer $[B_2O_{2.5-\delta}]_\infty$, namely, tetragonal pyramids and tetrahedra (Figure 1b), leading to a regular sequence (*-SBU2-SBU4-*).

The second [010] HREM image (Figure 7b) has been recorded for crystallites of the compound **#11**, with $p = 0.38$ (ED in Figure 3) and is typical of incommensurate modulated structures. At the level of the double layer $[B_2O_{2.5-\delta}]_\infty$ two bright dots alternate with 3 or 4 gray ones. A regular alternation of 3 and 4 gray dots in between the two bright dots (i.e., *SBU2-SBU3-SBU2-SBU4-*) would correspond to a commensurate modulation with $p = 4/11$. The excess of 3 gray dots (Figure 7b) with regard to the perfect [-3-4] alternation is consistent with the average value $4/11 < (p = 0.38) < 2/5$ and their insertion with an ad hoc period in the double layer $[B_2O_{2.5-\delta}]$ with the absence of short-range ordering.

(ii). Planar Defects. The formation of twinning domains, which results from the lowering in symmetry with regard to

dx.doi.org/10.1021/cm103635g |*Chem. Mater.* 2011, 23, 2786–2794

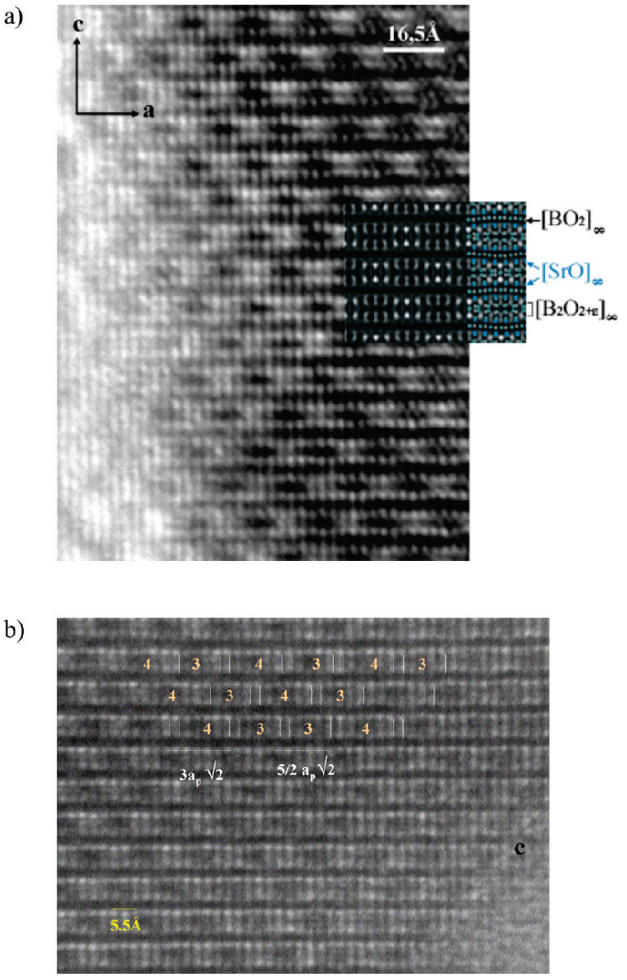

Figure 7. (a) Experimental and calculated [010] HREM images of a commensurate modulated crystal (**#8**), the brighter dots are correlated with the Sr positions. (b) [010] HREM image of the incommensurate modulated structure of **#11** (p = 0.38).

the ideal 2201-type subcell ($a_{id} = b_{id} = a_p\sqrt{2}$), generates contrast variation along $\vec{a}$ at the level of the double layer $[B_2O_{2.5-\delta}]_\infty$. Two large [010] and [100] oriented domains are shown in Figure 8a (**#8**); the twinning boundary (TB) is not coherent and appears in the form of a succession of short boundary segments, roughly parallel to the vector $\vec{t} = (1/p_1)\vec{a} + \vec{c}$ (p_1 = 0.38) and translated along $\vec{a}$. This orientation of the boundary can be linked to the different distortions of the BO_n polyhedra and the waving of the layers through their connection at the interface. Despite the small b/a discrepancy of the subcell parameters (varying between 1.004 and 1.008), these phenomena have been almost rarely observed in the ternary diagram, whatever the x and y values.

Intergrowth defects along $\vec{c}$ are also rarely observed. One example of a defective member m = 6 observed in the sample **#11** is given in Figure 8b; it corresponds to the intercalation of 6 adjacent perovskite-type layers in between two $[SrB_2O_{3.5-\delta}]_\infty$ RS blocks. Such a behavior was also reported for the two parent oxides $Sr_2Fe_3O_{6.46}$ and $Sr_2(Ga_{2/9}Co_{7/9})_3O_{6.33}$.[17,19] Note that this structural mechanism is different from those obtained for the series $Sr_{2-z}A_zFe_3O_{6.5-\delta}$ (with A = Bi, Tl, Ba, Pb, and La), in which the insertion of other cations in the Sr sites[25] is accommodated through intergrowth defects, contrary to the insertion of a great variety of B cations in the pure Sr based B-2201 framework.

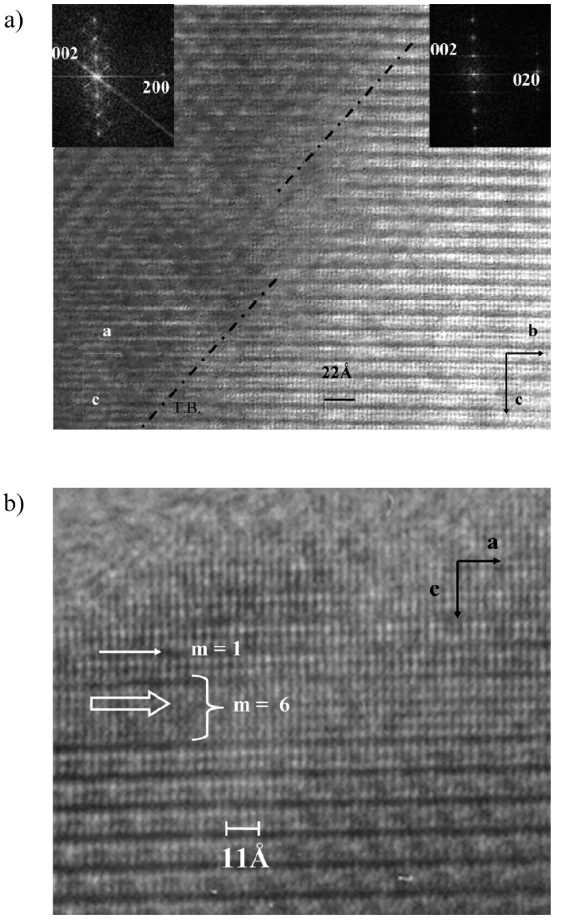

Figure 8. (a) [010] and [100] oriented domains (**#8**) and (b) **m** = 6 defective member (**#11**).

(III). Transport Properties. The transport measurements between 225 K and 400 K showed that the $(Sr,A')_2Fe_3O_{6.5-\delta}$ compounds exhibit a semiconducting behavior,[25] with a resistivity $\rho_{300\ K} \approx 10^4\ \Omega$ cm and activation energy close to 300 meV at 300 K (note that the resistivity values previously reported[22−24] cannot be directly compared because they have been measured at 800−900 °C). Their antiferromagnetic-like behavior was associated with a strong coupling at 180° ($Fe^{3+}-O-Fe^{3+}$) with high characteristic temperatures, ranging between 700 K and 800 K.[25]

Depending on the synthesis parameters (especially temperature and oxygen partial pressure), the intermediate $[Fe_2O_{2.5-\delta}]_\infty$ and $[Ga_{2/3}Co_{4/3}O_{2.5-\delta}]_\infty$ double layers of the RS block accommodate more or less oxygen, which is responsible for their large anion conductivity in the cobaltite. At present, the electrical conductivity of $Sr_2Ga_{2/3}Co_{7/3}O_{6.33}$ is too low to use this oxide as a thermoelectric material at high temperature in air ($\sigma_{300\ K}$ = 0.7 S cm^{-1}). Nonetheless, the significant lower electrical conductivity of $Sr_2Fe_3O_{6.5-\delta}$ indicates that the transport mechanism is different in ferrites and cobaltites. The high spin state of Co^{3+} ($t_{2g}^4e_g^2$), which makes the conduction in an e_g broad band, is assumed to be likely responsible of this difference, whereas the very stable high spin state configuration of trivalent iron ($t_{2g}^3e_g^2$) is much less favorable to the electronic delocalization.

The transport measurements of these B-2201′s have been carried out for the different points of the diagram, to understand the evolution of the magnetic and electronic properties versus the

dx.doi.org/10.1021/cm103635g |*Chem. Mater.* 2011, 23, 2786–2794

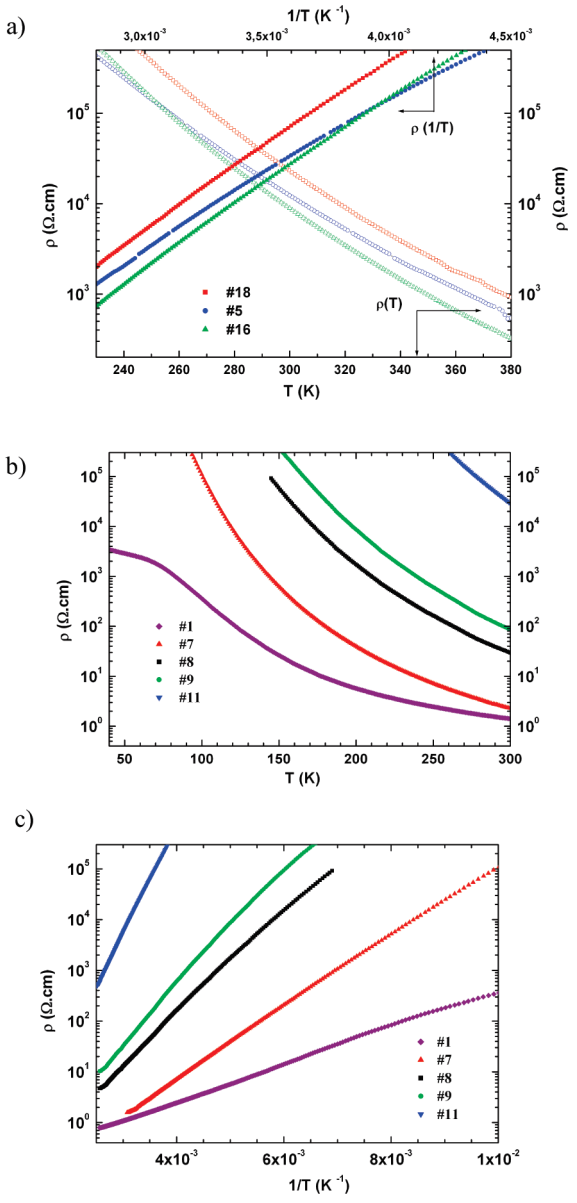

Figure 9. (a) T (lower x-scale) and $1/T$ (upper x-scale) dependencies of the electrical resistivity ρ for several Fe-rich compounds **#5**, **#16**, and **#18**. (b) $\rho(T)$ and (c) $\rho(1/T)$ curves for a Fe-rich compound (**#11**) and for compounds containing increasing (Co/Ga) content (from 1.38 for sample **#9** to 7/2 for sample **#1**) beyond the threshold (Co/Ga)/(Fe + Co + Ga) = 40%. A clear change in the magnitude of the activation energy is deduced from the change of slope of the $\rho(1/T)$ curves.

iron and cobalt ratio. In the studied T range, no magnetic field effect (up to 7 T) could be detected on the resistivity data.

(i). Electrical Conductivity. As above-mentioned, the electrical conductivity (σ) is much larger for the (Co/Ga) phase than that of the Fe-rich phase.[25] Accordingly, whatever the composition line in the ternary diagram is, σ increases as one starts from the pure Fe-composition (**#6**) toward the (Co/Ga) phases (**#1** to **#13**). However, this trend is not monotonic as shown in Figure 9a for the compositions with Fe/ΣB $\geq$ 0.6. For these compositions, the room temperature electrical resistivity (ρ) keeps values near 10^4 Ω cm with activation energies (E_A) near ~250 meV.

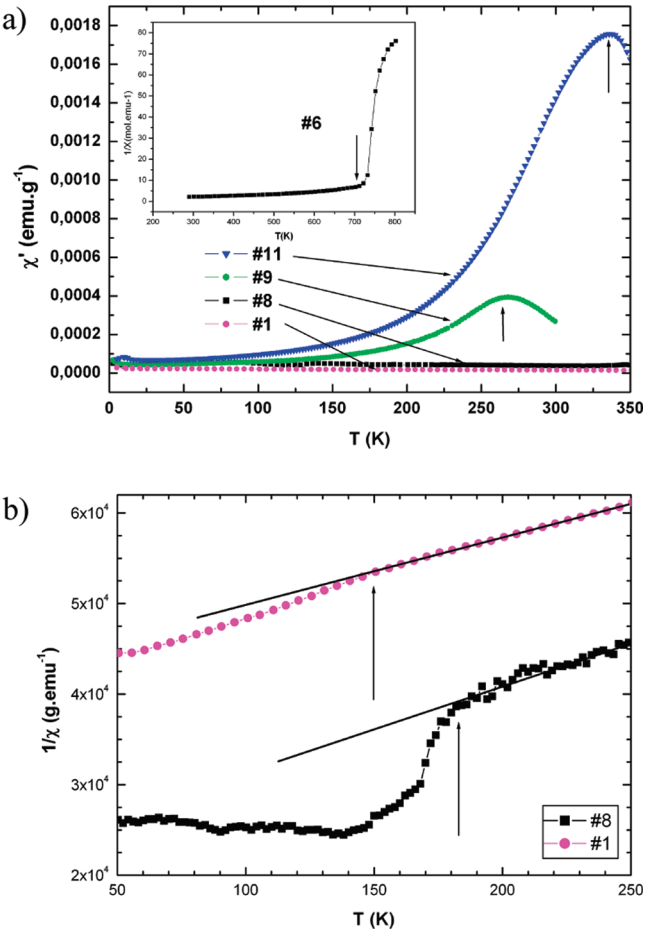

Figure 10. (a) $\chi'(T)$ curves increasing the Fe content from 0 (**#1**) to 2 (**#11**). $\chi^{-1}(T)$ curve for the Fe-2201 phase (**#6**) is given as an inset. (b) $\chi^{-1}(T)$ curves for the Co-2201 phase (**#1**) and for the compound **#8** ($Sr_2(FeCo_{1.3}Ga_{0.7})O_{6.5-\delta}$). The vertical arrows indicate the magnetic transition, which T increases with iron content.

By increasing further the (Co/Ga) content, ρ values decrease abruptly down to 10^2 Ω cm for compositions such as Fe/ΣB ≈ 0.6 as shown by the curves in Figure 9b. This change by more than 2 orders of magnitude can be understood as the creation of percolative -(Co−O−Co)- pathways and occurs in the zone where a cation rearrangement has been proposed to explain the cell parameters evolutions.

Such an interpretation is consistent with the values $\rho_{300\ K}$ ≈ 2.3 Ω cm and $\rho_{300\ K}$ ≈ 1.4 Ω cm for 16%-Fe and 0%-Fe, respectively. The fact that the charge hopping is ensured by the Co−O−Co network beyond about 40% of (Co/Ga) at the B site, is confirmed by the E_A values which are all close to ~100 meV (Figure 9c), that is, much smaller than the values found for the Fe-rich composition.

(ii). Magnetism. As shown in Figure 10a, the reciprocal magnetic susceptibility curves strongly differ for the end members Fe-2201 (**#6** with a magnetic transition at T_m = 750 K as shown in the inset of Figure 10a) and Co-2201 (**#1** with T_m ~ 150 K as shown in Figure 10b). Such behavior reflects the different magnetic exchanges for Fe^{3+}−O−Fe^{3+} and Co^{3+}(Ga^{3+})−O−Co^{3+}(Ga^{3+})-. As a consequence of such a difference, by diluting the Fe^{3+}−O−Fe^{3+} magnetic regions by (Co^{3+}/Ga^{3+}) substitution, it is found that the magnetic transition temperature decreases regularly

dx.doi.org/10.1021/cm103635g |*Chem. Mater.* 2011, 23, 2786–2794

from 750 K to ≈305 K for 25% of (Co/Ga) (#**11**) and then to 260 K for 45% of (Co/Ga) (# **9**). If one considers the much smaller χ^{-1} values for the Fe-rich phases (Figure 10a), it is obvious that the $Sr_2Fe_3O_{6.5-\delta}$ phase exhibits a ferromagnetic-like component, which is not present in the (Co/Ga) phase.

Thus, the effect of the (Co/Ga) substitution is double: *(i)* it dilutes the B−O−B magnetic interactions as Ga^{3+} is a d^{10} $S = 0$ cation and *(ii)* it creates disorder in the magnetic network implying also $Co^{3+}-O-Co^{3+}$ and $Fe^{3+}-O-Co^{3+}$ interactions unlike in the Fe-rich limit member. For the (Co/Ga)-2201 samples, the preferential occupation of the $S = 0$ Ga^{3+} cations in the double layers of the RS block is also probably hindering the magnetic coupling perpendicular to the perovskite layers. This might change the magnetic coupling from 3D to 2D along the (Co/Ga) for Fe substitution. Neutron diffraction experiments are now needed to allow the magnetic structure evolution to be established.

CONCLUSION

The investigation of the ternary diagram of $Sr_2Fe_{3-x}(Co_{x-y}Ga_y)O_{6.5-\delta}$ phases evidenced a large homogeneity domain of the B-2201-type phase, isostructural to the end members $Sr_2Fe_3O_{6.46}$[17] and $Sr_2Ga_{2/3}Co_{7/3}O_{6.33}$.[19] The coupled electron diffraction and energy dispersive spectroscopy analyses allowed the determination of the single phased domain obtained following two defined synthesis processes, but they also show its possible extension by non stoichiometry mechanisms and/or varying the processes. The electron diffraction study confirms that all the structures are modulated, in commensurate or incommensurate ways. The evolution of the subcell parameters, refined from X-ray powder diffraction data, and wavelength of the modulated structure show the effect of the joined introduction of Co and Ga in the $Sr_2Fe_3O_{6.5-\delta}$ phase upon the structures. Starting from $Sr_2Fe_3O_{6.46}$, a violation of the Vegard law through slope breakings is observed in the evolution of cell parameters and modulation vectors versus x. These variations are observed close to compositions with $Fe/\Sigma B \approx 0.6$ and assumed to be correlated with a rearrangement of the different B cations between the RS and perovskite layers. The refinements of XRD data recorded on different single crystals of the ternary diagram would shed light on this point. The HREM study showed that the most important source of disorder in the matrixes is associated with the sequence of polyhedra along $\vec{a}$, involving possible disproportionation or diffuse diffusion mechanisms. It is important to outline that twinning boundaries and intergrowth defects are rather rare phenomena despite the great variety of the B cations in the framework.

The study of physical properties, electrical conductivity and magnetic susceptibility, for the $Sr_2Fe_{3-x}(Co_{x-y}Ga_y)O_{6.5-\delta}$ compounds demonstrates that both properties can be changed in between those of the Fe and (Co/Ga) limit members. However, this change is not monotonic for the electrical conductivity as a (Co,Ga) content beyond the threshold value of $Fe/\Sigma B < 0.6$ is necessary to go from a transport characterized by an activation energy of the Fe-rich phase to that of the (Co,Ga)-rich phase. In that respect, this solid solution is of interest to study the electrical percolation effects and its coupling to the magnetic properties.

AUTHOR INFORMATION

Corresponding Author

*E-mail: sylvie.malo@ensicaen.fr.

REFERENCES

(1) Raveau, B.; Michel, C.; Hervieu, M.; Groult, D. *Crystal chemistry of High Tc superconducting copper oxides*, Springer Series in Materials Science 15; Springer-Verlag: New York, 1991, and references therein.

(2) R. H. Mitchell. *Perovskites modern and ancient*; Almaz Press Inc.: Thunder Bay, Ontario, Canada, 2002.

(3) Michel, C.; Hervieu, M.; Borel, M. M.; Grandin, A.; Deslandes, F.; Provost, J.; Raveau, B. *Z. Phys. B* **1987**, *68*, 421.

(4) Pelloquin, D.; Masset, A. C.; Maignan, A.; Michel, C.; Hervieu, M.; Raveau, B. *J. Solid State Chem.* **1999**, *148*, 108.

(5) Tarascon, J. M.; Miceli, P. F.; Barboux, P.; Hwand, D. M.; Dull, G. W.; Giroud, M.; Greene, L. H.; Lepage, Y.; Mckinnon, W. R.; Tselepis, E.; Pleizier, G.; Eibschutz, M.; Neumann, D. A.; Rhyne, J. J. *Phys. Rev. B* **1989**, *39*, 11587.

(6) Pelloquin, D.; Allix, M.; Michel, C.; Hervieu, M.; Raveau, B. *Phil. Mag.* **2001**, *81*, 1669.

(7) Pelloquin, D.; Maignan, A.; Hervieu, M.; Michel, C.; Raveau, B. *J. Solid State Chem.* **2000**, *151*, 210.

(8) Grebille, D.; Lepoittevin, Ch.; Malo, S.; Pérez, O.; Nguyen, N.; Hervieu, M. *J. Solid State Chem.* **2006**, *179* (12), 3849.

(9) Lepoittevin, C.; Malo, S.; Nguyen, N.; Hébert, S.; Van Tendeloo, G.; Hervieu, M. *Chem. Mater.* **2008**, *20*, 6468.

(10) Lepoittevin, C.; Malo, S.; Van Tendeloo, G.; Hervieu, M. *Solid State Sci.* **2009**, *11*, 595.

(11) Kanamaru, F.; Shimada, M.; Koizumi, M. *J. Phys. Chem. Solids* **1972**, *33*, 1169.

(12) Fjellvag, H.; Hauback, B. C.; Bredesen, R. *J. Mater. Chem.* **1997**, *7*, 2415.

(13) Mitchell, B. J.; Richardson, J. W.; Murphy, C. D.; Ma, B.; Balachandran, U.; Hodges, J. P.; Jorgensen, J. D. *J. Eur. Ceram. Soc.* **2002**, *22*, 661.

(14) Mellenne, B.; Retoux, R.; Lepoittevin, C.; Hervieu, M.; Raveau, B. *Chem. Mater.* **2004**, *16*, 5006.

(15) Rossell, D.; Abakumov, A. M.; Van Tendeloo, G.; Pardo, J. A.; Santiso *J. Chem. Mater.* **2004**, *16*, 2578.

(16) Lepoittevin, C.; Malo, S.; Nguyen, N.; Hébert, S.; Van Tendeloo, G.; Hervieu, M. *Chem. Mater.* **2008**, *20*, 6468.

(17) Pérez, O.; Mellenne, B.; Retoux, R.; Raveau., B.; Hervieu, M. *Solid State Sci.* **2006**, *8*, 431.

(18) Lepoittevin, C.; Malo, S.; Pérez, O.; Nguyen, N.; Maignan, A.; Hervieu, M. *Solid State Sci.* **2006**, *8*, 1294.

(19) Pelloquin, D.; Hébert, S.; Pérez, O.; Pralong, V.; Nguyen, N.; Maignan, A. *J. Solid State Chem.* **2005**, *178*, 792.

(20) Abakumov, A. M.; Rossel, M. D.; Yu, O.; Drozhzhin, O. A.; Leonova, S. L.; Dobrovolsky, Y. A.; Istomin, S. Y.; Van Tendeloo, G.; Antipov, E. *Chem. Mater.* **2008**, *20*, 4457.

(21) de Wolf, P. M. *Acta Crystallogr.* **1974**, *A30*, 777. de Wolf, P. M.; Jansenn, T.; Janner, A. *Acta Crystallogr.* **1981**, *A37*, 625.

(22) Patrakev, M. V.; Mitberg, E. B.; Leonodov, I. A.; Kozhevnidov, V. L. *Solid State Ionics* **2001**, *139*, 325.

(23) Waerenborg, J. C.; Rojas, D. P.; Vyshatko, N. P.; Shaula, A. L.; Kharton, V. V.; Marozau, I. P.; Naumovitch, E. N. *Mater. Lett.* **2003**, *57*, 3245.

(24) Ma, B.; Balachadran, U. *Solid State Ionics* **1997**, *100*, 53.

(25) Lepoittevin, C.; Malo, S.; Van Tendeloo, G.; Hervieu, M. *Solid State Sci.* **2009**, *11*, 595.